Highly Efficient Extremely Thin Absorber Solar Cells enabled by Cation Disorder Engineering

Yongjie Wang[1†], Seán R. Kavanagh[2,3†], Ignasi Burgués-Ceballos[1], Aron Walsh[3,4], David Scanlon[2,5], Gerasimos Konstantatos[1,6*]

[1]ICFO-Insitut de Ciencies Fotoniques, The Barcelona Institute of Science and Technology, Castelldefels, 08860 Barcelona, Spain.

[2]Thomas Young Centre and Department of Chemistry, University College London, London WC1H 0AJ, U.K.

[3]Thomas Young Centre and Department of Materials, Imperial College London, London SW7 2AZ, U.K.;

[4]Department of Materials Science and Engineering, Yonsei University, Seoul 03722, Republic of Korea.

[5]Diamond Light Source Ltd., Diamond House, Harwell Science and Innovation Campus, Didcot, Oxfordshire OX11 0DE, UK

[6]ICREA-Institució Catalana de Recerca i Estudia Avançats, Lluis Companys 23, 08010 Barcelona, Spain.

[†]These authors contributed equally to this work.

*e-mail: Gerasimos.Konstantatos@icfo.eu

Strong optical absorption of a semiconductor is a highly desirable property for a material to be considered in optoelectronic and photovoltaic applications. Strong light absorbers can enable ultrathin solar cells and photodetectors that in turn lead to significant reductions in cost, weight and manufacturing throughput as well as improve quantum efficiency and performance. The optimal thickness of a semiconductor absorber is primarily determined by its absorption coefficient. To date, this parameter has been considered as a fundamental material property and efforts to realize thinner photovoltaics have relied on light-trapping structures that add complexity and cost. Here, we demonstrate that by engineering cation disorder homogeneity in a ternary chalcogenide semiconductor leads to significant absorption increase due to enhancement of the optical transition matrix elements. We show that cation disorder engineered $AgBiS_2$ colloidal nanocrystals offer an absorption coefficient that is higher than any other photovoltaic material used to date, enabling highly efficient extremely thin absorber (ETA) photovoltaic devices. Leveraging this high absorption and by further optimization of the electron and hole blocking layers, we report solution-processed, environmentally-friendly, 30nm thick ETA solar cells with short circuit current density of 27 $mA \cdot cm^{-2}$, a

record power conversion efficiency of 9.17% (8.85% certified) and high stability under ambient conditions.

High-performance, lightweight solar cells featuring low cost and environmental friendliness have been a long-sought target in the photovoltaic field. Ultrathin solar cells can reduce material consumption and manufacturing demands, directly lowering the cost. Owing to an absorber thickness that is orders of magnitude lower than conventional solar cells, ultrathin solar cells further allow for flexible and light-weight form factors suited for building- or wearable- integrated photovoltaics. A thinner absorber layer also improves charge carrier collection and reduces bulk recombination, which are particularly prevalent in nanocrystalline solution-processed semiconductors[1,2], thus improving performance provided strong light absorption. Furthermore, high absorption in small absorber volumes allows for operating the device at high photo-generated carrier densities, a physical regime which maximizes the open-circuit voltage (V_{oc}) and permits advanced high-efficiency concepts such as hot-carrier solar cells[3].

Currently, high performance ultrathin solar cells are mainly realized via different light-trapping strategies, which are employed to compensate for the short circuit current drop due to incomplete absorption in the ultrathin absorbing layer[4,5]. The use of optical architectures, however, increases non-radiative recombination[4,6] and complicates the manufacturing process, introducing additional obstacles toward low-cost high-efficiency devices.

Typically, the absorption coefficient of a material determines the required thickness for optimal light harvesting under photovoltaic operation. The absorption coefficient of a semiconductor has been considered as a fundamental parameter of the material, with efforts to enhance light absorption in ultrathin absorbers relying on optical means[4,5]. We instead took the view - motivated by the fundamental relationship between atomic geometry, electronic structure and

optical absorption - that the absorption coefficient of a semiconductor can be tuned by engineering the atomistic material structure.

Cation disorder is a widely observed phenomenon in multinary materials, referring to the deviation of atomic positions in the cationic sublattice from an ordered crystalline arrangement. This phenomenon significantly impacts the optoelectronic properties of semiconductors[7–9] and has traditionally been considered an undesirable (and often unavoidable) effect, due to its entropically-driven nature[7,8,10,11]. Herein, we leverage the modulation of cation disorder homogeneity in multinary semiconductors as a pathway to enhancing optical transition matrix elements, in order to achieve improved absorption coefficient and photovoltaic device efficiency.

Cation disorder homogeneity and absorption behaviour

In this work, we focus on ternary $AgBiS_2$ nanocrystals (NCs), a solution-processed nanomaterial comprising environmentally-friendly elements[12,13] with reported efficiencies exceeding 6% in thin-film solar cells[1,14]. The cation distribution around Ag sites in $AgBiS_2$ nanocrystals has shown evidence for non-random Ag-Ag correlation[15], indicating the presence of inhomogeneous cation disorder (i.e. cation segregation with local Ag-rich and Bi-rich regions), likely due to growth kinetics during synthesis and surface ligand interactions[16–18].

An illustration of inhomogeneous cation disorder within $AgBiS_2$ NCs is shown in Fig. 1a. The valence band maximum (VBM) of $AgBiS_2$ primarily derives from Ag *d* and S *p* states, while the conduction band minimum (CBM) arises from Bi *p* and S *p* interactions[19,20] (Fig. 1b). A clear spatial separation of the Ag-derived VBM and Bi-derived CBM for the cation-segregated configuration can be observed in the local electronic density of states (LDOS), shown in Fig. 1c. In contrast, under homogeneous cation disorder, we predict a VBM and CBM delocalized

over the entire material (Fig. 1d), with the correlation between cation distribution and spatial (de)localization of the band extrema further demonstrated by Fig. 1e.

The theoretically simulated absorption spectra of $AgBiS_2$ for both inhomogeneous and homogenous cation disorder are provided in Fig. 2a. As expected, we find a substantially increased transition dipole matrix element (Supplementary Fig. 1) and thus enhanced optical absorption upon homogenizing disorder.

To experimentally tune cationic disorder, we first assessed the thermodynamics of atomic reordering, in particular the formation energy difference needed to induce disorder. Density Functional Theory (DFT) was employed to calculate the inter-site cation exchange energy. Under the highest level of theory employed for phase energetics (hybrid DFT including spin-orbit coupling effects), the bulk order-disorder enthalpy difference is calculated as 17.4 meV/atom, indicating the accessibility of cation site-swapping in $AgBiS_2$ under mild annealing conditions. Considering the low inter-site cation exchange energy in $AgBiS_2$, we sought to anneal $AgBiS_2$ NCs under low-temperature conditions to facilitate cation inter-site exchange and thus an entropically-driven transition to homogenous cation distribution. Fig. 2b plots the absorption coefficient of our NC films upon annealing under different temperatures. Comparing Fig. 2a and 2b, the simulated absorption spectrum for cation segregation configurations (inhomogeneous disorder) matches well with the as-prepared $AgBiS_2$ NC film, both exhibiting Urbach tailing at longer wavelengths, which is pernicious for photovoltaic devices[21,22]. However, in the homogenous cation-disordered structure, the simulated absorption coefficient is much higher than the cation-segregated case, with reduced band tailing, manifesting favourable properties for optoelectronic applications[23]. As shown in Fig. 2b, the absorption coefficient of $AgBiS_2$ NCs films is enhanced by up to a factor of two after annealing, alongside reduced band tailing, as predicted by *ab initio* calculations. With this low-energy and scalable annealing process, we produce a semiconducting material that exhibits an absorption

coefficient 5-10 times greater than any other material currently used in photovoltaic technology[4,24–28], across a wide spectral range from 400 – 1000 nm (Fig. 2c).

With the high absorption coefficient of our films, an ultrathin layer of $AgBiS_2$ NCs would be sufficient to absorb most of the light in the visible range. In order to assess the potential of our strongly-absorbing NC films, we calculate the maximum achievable short-circuit current density J_{sc} using the transfer matrix method[29,30], assuming 100% internal quantum efficiency (Supplementary Fig. 2). Fig. 2d plots the maximum J_{sc} as a function of the active layer thickness for different annealing temperatures, corresponding to varying degrees of cation disorder homogeneity. Upon increased annealing temperature, we witness an increase in J_{sc} reached at low active layer thicknesses (t < 200 nm). We predict a maximum J_{sc} of 28 (32) $mA \cdot cm^{-2}$ for $AgBiS_2$ NCs films annealed at 115°C (150°C), with thicknesses of only 30 nm. Furthermore, the Spectroscopic Limited Maximum Efficiency (SLME) was calculated assuming only radiative recombination in devices[31]. As shown in Fig. 2e, a high photovoltaic efficiency up to 26% was predicted for a 30 nm absorber layer, indicating the exceptional performance potential of ultrathin solar cells based on $AgBiS_2$ NC films.

Cation configuration transition

To further verify the proposed cation homogenization as the underlying mechanism responsible for the optical absorption enhancement in $AgBiS_2$ NC films, we used X-Ray Diffraction (XRD) and Transmission Electron Microscopy (TEM) to probe the changes in crystal structure upon annealing. Interestingly, while XRD analysis suggested increased crystallite size (from 4.2 nm to 6.2 nm) upon annealing at 115°C, High Resolution Transmission Electron Microscopy (HRTEM) showed no measurable size differences in these samples (Supplementary Fig. 3). The sharpening of XRD peaks despite negligible NC growth indicates an increase in crystallinity due to atomic rearrangements within the nanocrystals. Further increasing the

annealing temperature to 150℃ and 200℃ causes NCs to fuse to larger crystals (28 nm and 47 nm, Supplementary Fig. 3c). Point defects are observable from HRTEM after high temperature annealing, which could be harmful for optoelectronic applications[32] (Supplementary Fig. 4). In addition to peak narrowing in XRD patterns, the peak positions were also found to shift to higher angles upon annealing (Fig. 3a). To deconvolute the effect of crystal size and cation arrangement, we calculated the expected XRD patterns for homogeneously disordered cubic $AgBiS_2$ (space group $Fm\bar{3}m$), with crystal size as the only variable parameter (Supplementary Fig. 5). The full width half maximum (FWHM) of all peaks sharpens with crystal growth, while the peak positions remain essentially the same, as expected. However, transitioning from cation-segregated configurations to homogeneous cation disorder, while fixing the crystallite size, the simulated XRD patterns of $AgBiS_2$ show distinct peak shifts to higher angles as well as peak narrowing (Fig. 3b), matching the experimental observations upon annealing. The XRD peak shifts primarily originate from the shortening of Ag-S bond lengths, while peak narrowing occurs due to narrowing of the bond length distribution, upon homogenization of the cation distribution (Supplementary Fig. 6). This phenomenon was further confirmed with HRTEM measurements, as shown in Fig. 3c and d, with integrated line profiles of the {200}-plane showing a slight shrinkage after annealing, further confirming the transition from cation segregation to homogeneous disorder.

Considering the difference in local bonding environments for different cation configurations, changes in Madelung potential were expected[33]. We calculate the average Madelung potential at Bi sites as 3.29 V and 4.66 V for segregated and homogeneous cation configurations, respectively, using Bader atomic charges. A greater Madelung potential suggests a decrease in XPS binding energy, upon transitioning from inhomogeneous to homogeneous cation disorder[33,34]. As shown in Fig. 3e, the Bi 5*d* peaks in the simulated XPS spectra are noticeably shifted to lower binding energies for homogeneous cation disorder, as compared to cation-

segregated configurations. Likewise, the annealed $AgBiS_2$ NCs show a small but significant chemical shift to lower energy, compared with as-prepared samples (Fig. 3f and g), in agreement with our proposition of cation homogenization upon annealing.

Ultrathin $AgBiS_2$ NC solar cells

Having developed a material with such strong optical absorption, we next sought to produce highly efficient ultrathin solution-processed solar cells with these nanocrystals. Solar cells were fabricated with an architecture of Glass/ITO/SnO_2/$AgBiS_2$/HTL/MoO_3/Ag, as shown in Fig. 4a. Cross-sectional Transmission Electron Microscopy (TEM) confirms the ultrathin nature of the device layers (Fig. 4b). We first used PTB7 as an electron blocking layer, in accordance with previous studies[1,14]. The devices showed an average power conversion efficiency (PCE) of 6.4 ± 0.6%, with a champion device reaching PCE of 7.6% (Table 1) – higher than the previously reported record performance of 6.3%[1,14,35–37]. Atomic Force Microscopy (AFM) revealed a surface roughness of 0.6 nm for a 4 nm PTB7 film (Supplementary Fig. 7), which undermines the performance of the cells by introducing interface recombination[38]. We sought to replace PTB7 with an alternative electron-blocking layer with improved morphological characteristics. We found that PTAA yielded improved uniformity (RMS roughness of 0.4 nm) leading to significant improvement in V_{oc} and fill factor (FF) (Supplementary Fig. 7), and resulting in a ~20% increase in power conversion efficiency to 8.7 ± 0.3%, with a best device reaching 9.17% (Fig. 4c and d). One of our champion devices was sent to an accredited PV calibration laboratory (Newport, USA), which certified a PCE of 8.85% under AM1.5G full sun illumination, with negligible hysteresis (Fig. 4e, Supplementary Fig. 8). The measured J_{sc} of 27 $mA \cdot cm^{-2}$ matched well with the predicted value from optical modelling, and was further confirmed by the external quantum efficiency (EQE) spectrum, which gives a value of 26.5 $mA \cdot cm^{-2}$ (Fig. 4f).

To assess the stability of our $AgBiS_2$ NC solar cells, we first measured their shelf lifetime by storing the un-encapsulated devices in ambient conditions with a temperature of ~25℃ and relative humidity of ~30%. The device retained its original performance after four months' aging (Supplementary Fig. 9). The operational stability was further investigated by subjecting the un-encapsulated device to AM1.5G one sun illumination in ambient atmosphere with relative humidity ~ 60%. The device performance was measured by applying a forward bias fixed at the maximum power point (MPP). As shown in Fig. 4g, the PCE of the PTB7 device dropped below 2% after 20 minutes illumination, while the PTAA device demonstrated much better operational stability under continuous operation. After 10 hours MPP testing on non-encapsulated devices in ambient conditions, the device retained 85% of its original efficiency. To our knowledge the devices reported herein set a record among low-temperature and solution-processed, non-toxic inorganic solar cells in terms of stability and performance[39–42]. These results support that $AgBiS_2$ NCs is extremely promising material for low-cost, efficient, stable and environmentally friendly solar cells.

In conclusion, we have demonstrated that the absorption coefficients of ternary $AgBiS_2$ NCs can be enhanced via cation disorder homogenization at mild annealing conditions. Ultra-high absorption coefficients were obtained in annealed $AgBiS_2$ NC films, with a calculated SLME of over 26% for a 30 nm NC film. The transition in cation configuration was further confirmed by the combination of *ab initio* calculations with XRD, HRTEM and XPS measurements. Ultrathin solar cells are fabricated based on ultra-absorbing $AgBiS_2$ NCs. A high J_{sc} of 27 $mA \cdot cm^{-2}$ and a record efficiency up to 9.17% were obtained with an independent certification of 8.85% from Newport. The air stability and photostability was also recorded in high performance devices. Our work not only establishes the extraordinary potential of ultrathin $AgBiS_2$ NC solar cells, which are solution-processable and RoHS-compliant, but also

demonstrates the importance and power of atomic configuration engineering in multinary systems.

Methods

Density Functional Theory (DFT) simulations. The AiiDA infrastructure was used to maintain data provenance for all calculations performed in this study[43]. Calculations were performed using Density Functional Theory (DFT) within periodic boundary conditions through the Vienna *Ab Initio* Simulation Package (VASP)[44–46]. Using the projector-augmented wave method, scalar-relativistic potentials were employed to describe the interaction between core and valence electrons.[47] Calculations were carried out using Γ-centred k-point meshes with a reciprocal space sampling of 0.11 $Å^{-1}$ and a plane-wave kinetic energy cutoff of 300 eV (increased to 450 eV for structural relaxations, to avoid the possibility of Pulay stress). With these parameter choices, the ground-state energies of all known structures in the Ag-Bi-S system were converged to within 1 meV/atom.

Cation Disorder. To model the effects of varying degrees of cation order/disorder, two approaches were employed. Firstly, to simulate total random cation disorder, a 64-atom supercell for $AgBiS_2$ in the $Fm\bar{3}m$ rocksalt structure was generated using the special quasi-random structure (SQS) method[48], in which the cation-cation cluster correlations are optimised to obtain the best approximation to an ideal infinite random distribution for a given supercell. Here, the Alloy Theoretic Automated Toolkit (ATAT)[49] was used to generate the SQS supercell via Monte-Carlo simulated annealing loops[50]. Eight Monte-Carlo simulations were performed, with the structure giving the best match to the true disordered solid solution chosen for further calculations. This corresponded to an 'objective function' of -81.18; considering 2-atom

clusters up to 12 Å separation, 3-atom clusters up to maximum 10 Å pair separation and 4-atom clusters up to 8 Å pair separation (using the experimental rocksalt crystal structure)[37].

The screened hybrid DFT exchange-correlation functional of Heyd, Scuseria and Ernzerhof (HSE06)[38] was used to calculate the structural and electronic properties of $Fm\bar{3}m$ (using this SQS structure) and $R\bar{3}m$ $AgBiS_2$, unless otherwise stated, having been demonstrated to accurately predict the electronic structures of semiconductor materials[53,54]. To account for relativistic effects, due to the presence of heavy-atom elements Ag and Bi, spin–orbit coupling effects were included in all electronic and optical calculations (HSE06+SOC).

Secondly, to investigate the effects of both partial order and inhomogeneous disorder (i.e. cation segregation with Ag-rich and Bi-rich regions) on the cation sublattice, all possible configurations for $AgBiS_2$ in a 32-atom rocksalt structure were enumerated using the Transformer package[55], yielding 440 symmetry-inequivalent arrangements. Here, the PBEsol[42] semi-local exchange-correlation functional was used for geometry optimisations and energetic analysis, motivated by its well-established accuracy for the structural relaxation of bulk solids[43] and moderate computational cost. Moreover, this functional was tested against both experiment and the computationally-intensive HSE06 hybrid DFT functional for bulk geometry optimisation and energetics respectively, using all known structures in the Ag-Bi-S system. Here, PBEsol was found to accurately reproduce experimentally-reported crystal structures, with a mean absolute error <1.5% in the lattice parameters, as well as reproducing the energetic ordering of phases on the convex hull according to both HSE06 and experiment.

To ensure consistency when comparing the results of these calculations to that of $Fm\bar{3}m$ (SQS) $AgBiS_2$, a new 32-atom SQS supercell was generated using the same procedure as outlined above, and relaxed with PBEsol. In this case, a perfect 'objective function' match to the true disordered solution was obtained. While appropriate for structural and energetic analysis of cation configurations in $AgBiS_2$, semi-local DFT is known to severely underestimate electronic

bandgaps[58,59], and so the HSE06+SOC hybrid DFT functional was used to calculate the optical and electronic properties of these configurations. In this case, down-sampling of the Fock exchange matrix by a factor of 2 (NKRED = 2) was employed to reduce the computational cost to a manageable level. This choice was confirmed to affect the electronic bandgap by <0.05 eV for the 32-atom SQS supercell.

To investigate the impact of supercell size on the calculated properties, the 32-atom SQS supercell was also relaxed with the HSE06 functional, to then compare with the 64-atom structure. The total energy was found to match that of the 64-atom SQS supercell to <1 meV/atom, while the bandgap was found to increase slightly from 0.69 eV to 0.83 eV for the 32-atom supercell.

Post-processing. Primitive and unfolded electronic band structure diagrams were generated using sumo and PyVaspWfc[46,47] respectively. Effmass was used to calculate carrier effective masses[62], and photoemission spectra were generated using Galore[63]. COHP analysis and charge-density partitioning was performed using LOBSTER,[50] and the vasppy package[51] was used to calculate radial distribution functions. The pymatgen package was used throughout for manipulation and analysis of calculation inputs and outputs[66].

Chemicals and materials. Reagents were purchased from Sigma Aldrich, except SnO_2 colloid precursor (tin (IV) oxide, 15% in H_2O colloidal dispersion), which was obtained from Alfa Aesar. Poly (triaryl amine) (PTAA) was purchased from EM index and Poly [[4,8-bis[(2-ethylhexyl)oxy]benzo[1,2-b:4,5-b']dithiophene-2,6-diyl][3-fluoro-2-[(2-ethylhexyl) carbonyl] thieno [3,4-b]thiophenediyl]] (PTB7) was purchased from 1-materials.

Synthesis of $AgBiS_2$ nanocrystals. The Schlenk technique was used to synthesize $AgBiS_2$ nanocrystals, following previous report with modifications[1,14]. 4 mmol $Bi(OAc)_3$, 3.2 mmol Ag(OAc), 24 mL oleic acid (OA) and 15 mL 1-octadecene (ODE) was pumped at 100°C for 2 hours (~0.2 mbar) to remove oxygen and moisture. 4 mmol hexamethyldisilathiane (HMS)

dissolved in 5 mL ODE was quickly injected into the flask. The heating mantel was removed and the reaction was cooled down with water bath for ~5 min. After that, the crude solution was left stirring for 1 hour at room temperature. The nanocrystals were isolated by adding acetone, followed by centrifugation. The extracted nanocrystals were re-dispersed in toluene and acetone was added to precipitate nanocrystals. The re-dispersion/precipitation was repeated once more. Finally, the obtained $AgBiS_2$ nanocrystals powder was dispersed in anhydrous toluene (20 mg mL^{-1}) and stored in ambient atmosphere for device fabrication.

Characterization of $AgBiS_2$ nanocrystals and films. Films exchanged with 3-mercaptopropionic acid (3-MPA) were grown on glass substrates, followed by annealing at different temperatures in glovebox. The thicknesses were measured using a profilometer. The complex refractive index was measured at various angles using broadband Sopra Ellipsometer GES5E. The software SEMILAB Spectroscopic Ellipsometry Analyzer was utilized to fit a model of stacked layers of appropriate optical constants and the thickness from profilometer was used as an input. The absorption coefficients are calculated from extinction coefficients. XRD data were collected using a Rigaku Smartlab powder diffractometer in Bragg-Brentano geometry with Cu Kα radiation. XPS measurements was performed with a SPECS PHOIBOS 150 hemispherical analyser (SPECS GmbH, Berlin, Germany) in ultra-high vacuum conditions (10^{-10} mbar), with a monochromatic Kα x-ray source (1486.74 eV) at the Institut Catala de Nanociencia i Nanotecnologia (ICN2). TEM was performed at the Scientific and Technological Centres of the University of Barcelona (CCiT-UB). TEM images were obtained using a JEOL 2100 microscope operating at an accelerating voltage of 200 kV.

Optical modelling and Spectroscopic limited maximum efficiency. A homemade MATLAB code was used to implement the transfer matrix formalism. We assumed that each layer was flat and considered no scattering effects. Short circuit current density was calculated with the

assumption of 100% internal quantum efficiency. Spectroscopic Limited Maximum Efficiency (SLME) was calculated according to:

$$SLME = P_{max}$$

$$P = -V * \left\{ J_0 \left[\exp\left(\frac{eV}{kT}\right) - 1 \right] - J_{sc,TMM} \right\}$$

where *e* the elementary charge, *k* the Boltzmann constant, *T* the temperature, and J_0 the dark saturation current density, calculated with the assumption of only radiative recombination:

$$J_0 = e * \int_0^{+\infty} EQE_{TMM} * \emptyset_{BB}(E)\, dE$$

where EQE_{TMM} is the calculated total absorption in $AgBiS_2$ NCs layer, and $\emptyset_{BB}$ is the black body radiation spectra at 300 K.

Solar cell fabrication. All solar cell fabrication steps were performed in ambient air, unless with specific descriptions. ITO covered glass substrates (Universität Stuttgart, Institut für Großflächige Mikroelektronik) were cleaned by ultra sonication in soapy water, acetone and isopropanol for 20 min each and dried with nitrogen, followed with 0.5 h UV/Ozone treatment. SnO_2 electron transport layer was then spin cast from diluted Alfa SnO_2 colloid solution (1:5.6 v/v with H_2O) with spin speed of 2000 rpm and annealed at 270°C for 15 min. Afterwards, three layers of $AgBiS_2$ nanocrystals were deposited from 20 mg mL^{-1} toluene solution via layer-by-layer (LbL) method. For each $AgBiS_2$ nanocrystals layer, one drop of $AgBiS_2$ NCs solution was spin-coated onto SnO_2/ITO substrates during spinning (2000 rpm). 3-Mercaptopropionic acid (MPA)/methanol (1% v/v) solution was then applied to the nanocrystals film for 45s, followed by two rinse-spin steps with methanol and once with toluene. The films were transferred into glovebox for 10 min annealing at 115°C and then stored in dry air before spin-coating PTB7 (5 mg mL^{-1} in dichlorobenzene) or PTAA solution (2 mg mL^{-1} in toluene) at

3000 rpm. Finally, a Kurt J. Lesker Nano36 system was used to deposit 3 nm of MoO_3 and 120 nm of Ag through a shadow mask to produce solar cells with a diameter of 2 mm (area of 3.14 mm^2).

Solar cell characterization. All device characterization was performed in air under ambient conditions. Current-voltage measurements were performed with a Keithyley 2400 Sourcemeter and a Newport Oriel Sol3A solar simulator with an AM1.5G filter. The intensity of the solar light was calibrated using a Hamamatsu S1336 silicon photodiode that had been calibrated at the Fraunhofer Institute of Solar Energy Systems, Freiburg, Germany. The solar cells were measured with and without masks, and slightly lower V_{oc} was observed when measuring with masks, due to masking effect. For certified cells, appropriate masks have always been used. The EQE was measured using a Newport Cornerstone 260 monochrometer, a Thorlabs MC2000 chopper, a Stanford Research SR570 trans-impedance amplifier and a Stanford Research SR830 lock-in amplifier. A calibrated Newport 818-UV photodetector was used as a reference. Shelf stability was obtained from devices stored in air without encapsulation. For the maximum power point (MPP) measurement, the MPP voltage (t = 0) was measured before MPP testing. The device was then held at the MPP voltage (t = 0) for operating stability test. The device was unencapsulated under AM1.5G illumination. All devices were characterized under ambient condition with relative humidity > 60% and ambient temperature ~25℃.

Acknowledgements

The authors acknowledge financial support from the European Research Council (ERC) under the European Union's Horizon 2020 research and innovation programme (grant agreement no. 725165) and the Fundació Joan Ribas Araquistain (FJRA). This project was supported also by Fundació Privada Cellex, the program CERCA, EQC2019-005797-P (AEI/FEDER UE) and

"Severo ochoa" Center of Excellence CEX2019-000910-S – Funded by the Spanish State Research Agency. I. Burgués-Ceballos acknowledges support from the Government of Catalonia's Beatriu de Pinós postdoctoral programme (grant number 2017BP00241). This project has received funding from the European Union's Horizon 2020 research and innovation programme under the Marie Skłodowska-Curie grant agreement No. 754558. Seán R. Kavanagh thanks Liam Harnett-Caulfield for help with using the ATAT software package, Dr. Yong-Seok Choi for help with calculating the Madelung potentials and acknowledges the EPSRC Centre for Doctoral Training in the Advanced Characterisation of Materials (CDT-ACM)(EP/S023259/1) for funding a PhD studentship. We acknowledge the use of the UCL Kathleen High Performance Computing Facility (Kathleen@UCL), the Imperial College Research Computing Service, and associated support services, in the completion of this work. Via membership of the UK's HEC Materials Chemistry Consortium, which is funded by the EPSRC (EP/L000202, EP/R029431, EP/T022213), this work used the ARCHER2 UK National Supercomputing Service and the UK Materials and Molecular Modelling (MMM) Hub (Thomas – EP/P020194 & Young – EP/T022213). DOS acknowledges support from the EPSRC (EP/N01572X/1) and from the European Research Council, ERC (Grant No. 758345).

Author contributions

G.K. supervised and directed the study. Y.W. and G.K. conceived the idea, designed this study and co-wrote the manuscript with feedback from co-authors. Y.W. synthesized the $AgBiS_2$ NCs, performed material characterization, fabricated, characterized the solar cells, and analysed the data, with the help of I.B. Y.W. did the optical modelling. S.K. designed and conducted the theoretical modelling, analysed the DFT simulations, interpreted the data, provided insights and contributed to manuscript writing. D.O.S and A.W. supervised the theoretical modelling.

Additional information

Supplementary information is available in the online version of the paper. Correspondence and request materials should be addressed to G.K.

Data and code availability

The data and code that supported the current study are available from the corresponding author on request.

Competing financial interests

The authors declare no competing financial interests.

References

1. Bernechea, M. *et al.* Solution-processed solar cells based on environmentally friendly AgBiS2 nanocrystals. *Nat. Photonics* **10**, 521–525 (2016).

2. Boles, M. A., Ling, D., Hyeon, T. & Talapin, D. V. The surface science of nanocrystals. *Nat. Mater.* **15**, 364–364 (2016).

3. Green, M. A. & Bremner, S. P. Energy conversion approaches and materials for high-efficiency photovoltaics. *Nat. Mater.* **16**, 23–34 (2017).

4. Massiot, I., Cattoni, A. & Collin, S. Progress and prospects for ultrathin solar cells. *Nat. Energy* **5**, 959–972 (2020).

5. Chen, H.-L. *et al.* A 19.9%-efficient ultrathin solar cell based on a 205-nm-thick GaAs absorber and a silver nanostructured back mirror. *Nat. Energy* **4**, 761–767 (2019).

6. Adhyaksa, G. W. P., Johlin, E. & Garnett, E. C. Nanoscale Back Contact Perovskite Solar Cell Design for Improved Tandem Efficiency. *Nano Lett.* **17**, 5206–5212 (2017).

7. Bosson, C. J. *et al.* Cation disorder and phase transitions in the structurally complex solar cell material Cu2ZnSnS4. *J. Mater. Chem. A* **5**, 16672–16680 (2017).

8. Chen, W., Dahliah, D., Rignanese, G.-M. & Hautier, G. Origin of the low conversion efficiency in Cu_2ZnSnS_4 kesterite solar cells: the actual role of cation disorder. *Energy Environ. Sci.* **14**, 3567–3578 (2021).

9. Malerba, C., Valentini, M. & Mittiga, A. Cation Disorder In Cu2ZnSnS4 Thin Films: Effect On Solar Cell Performances. *Sol. RRL* **1**, 1700101 (2017).

10. Li, J. *et al.* Defect Control for 12.5% Efficiency Cu2ZnSnSe4 Kesterite Thin-Film Solar Cells by Engineering of Local Chemical Environment. *Adv. Mater.* **n/a**, 2005268.

11. Zawadzki, P., Zakutayev, A. & Lany, S. Entropy-Driven Clustering in Tetrahedrally Bonded Multinary Materials. *Phys. Rev. Appl.* **3**, (2015).

12. Mohan, R. Green bismuth. *Nat. Chem.* **2**, 336–336 (2010).

13. Vesborg, P. C. K. & Jaramillo, T. F. Addressing the terawatt challenge: scalability in the supply of chemical elements for renewable energy. *RSC Adv.* **2**, 7933 (2012).

14. Burgués-Ceballos, I., Wang, Y., Akgul, M. Z. & Konstantatos, G. Colloidal AgBiS2 nanocrystals with reduced recombination yield 6.4% power conversion efficiency in solution-processed solar cells. *Nano Energy* **75**, 104961 (2020).

15. Kopula Kesavan, J. *et al.* Cation Disorder and Local Structural Distortions in AgxBi1–xS2 Nanoparticles. *Nanomaterials* **10**, 316 (2020).

16. Schnepf, R. R. *et al.* Utilizing Site Disorder in the Development of New Energy-Relevant Semiconductors. *ACS Energy Lett.* **5**, 2027–2041 (2020).

17. Yang, W.-C., Miskin, C. K., Carter, N. J., Agrawal, R. & Stach, E. A. Compositional Inhomogeneity of Multinary Semiconductor Nanoparticles: A Case Study of Cu_2ZnSnS_4. *Chem. Mater.* **26**, 6955–6962 (2014).

18. Hao, M. *et al.* Ligand-assisted cation-exchange engineering for high-efficiency colloidal Cs1−xFAxPbI3 quantum dot solar cells with reduced phase segregation. *Nat. Energy* **5**, 79–88 (2020).

19. Ju, M.-G., Dai, J., Ma, L., Zhou, Y. & Zeng, X. C. $AgBiS_2$ as a low-cost and eco-friendly all-inorganic photovoltaic material: nanoscale morphology–property relationship. *Nanoscale Adv.* **2**, 770–776 (2020).

20. Viñes, F., Bernechea, M., Konstantatos, G. & Illas, F. Matildite versus schapbachite: First-principles investigation of the origin of photoactivity in AgBi S 2. *Phys. Rev. B* **94**, 235203 (2016).

21. Liu, M. *et al.* Hybrid organic–inorganic inks flatten the energy landscape in colloidal quantum dot solids. *Nat. Mater.* **16**, 258–263 (2017).

22. Kagan, C. R. & Murray, C. B. Charge transport in strongly coupled quantum dot solids. *Nat. Nanotechnol.* **10**, 1013–1026 (2015).

23. Wong, J., Omelchenko, S. T. & Atwater, H. A. Impact of Semiconductor Band Tails and Band Filling on Photovoltaic Efficiency Limits. *ACS Energy Lett.* **6**, 52–57 (2021).

24. Treharne, R. E. *et al.* Optical Design and Fabrication of Fully Sputtered CdTe/CdS Solar Cells. *J. Phys. Conf. Ser.* **286**, 012038 (2011).

25. ElAnzeery, H. *et al.* Refractive index extraction and thickness optimization of Cu2ZnSnSe4 thin film solar cells. *Phys. Status Solidi A* **212**, 1984–1990 (2015).

26. *Handbook of optical constants of solids*. (Academic Press, 1998).

27. Manzoor, S. *et al.* Optical modeling of wide-bandgap perovskite and perovskite/silicon tandem solar cells using complex refractive indices for arbitrary-bandgap perovskite absorbers. *Opt. Express* **26**, 27441 (2018).

28. Chen, C. *et al.* Characterization of basic physical properties of Sb2Se3 and its relevance for photovoltaics. *Front. Optoelectron.* **10**, 18–30 (2017).

29. Pettersson, L. A. A., Roman, L. S. & Inganäs, O. Modeling photocurrent action spectra of photovoltaic devices based on organic thin films. *J. Appl. Phys.* **86**, 487–496 (1999).

30. Centurioni, E. Generalized matrix method for calculation of internal light energy flux in mixed coherent and incoherent multilayers. *Appl. Opt.* **44**, 7532 (2005).

31. Guillemoles, J.-F., Kirchartz, T., Cahen, D. & Rau, U. Guide for the perplexed to the Shockley–Queisser model for solar cells. *Nat. Photonics* **13**, 501–505 (2019).

32. Gilmore, R. H. *et al.* Epitaxial Dimers and Auger-Assisted Detrapping in PbS Quantum Dot Solids. *Matter* **1**, 250–265 (2019).

33. Bagus, P. S., Illas, F., Pacchioni, G. & Parmigiani, F. Mechanisms responsible for chemical shifts of core-level binding energies and their relationship to chemical bonding. *J. Electron Spectrosc. Relat. Phenom.* **100**, 215–236 (1999).

34. Tambo, T. & Tatsuyama, C. XPS Study on the Chemical Shifts of Crystalline III–VI Layered Compounds. *J. Phys. Soc. Jpn.* **54**, 4382–4389 (1985).

35. Akgul, M. Z., Figueroba, A., Pradhan, S., Bi, Y. & Konstantatos, G. Low-Cost RoHS Compliant Solution Processed Photovoltaics Enabled by Ambient Condition Synthesis of $AgBiS_2$ Nanocrystals. *ACS Photonics* **7**, 588–595 (2020).

36. Hu, L. *et al.* Enhanced optoelectronic performance in $AgBiS_2$ nanocrystals obtained *via* an improved amine-based synthesis route. *J. Mater. Chem. C* **6**, 731–737 (2018).

37. Oh, J. T. *et al.* Water-resistant $AgBiS_2$ colloidal nanocrystal solids for eco-friendly thin film photovoltaics. *Nanoscale* **11**, 9633–9640 (2019).

38. Pan, H. *et al.* Advances in design engineering and merits of electron transporting layers in perovskite solar cells. *Mater. Horiz.* 10.1039.D0MH00586J (2020) doi:10.1039/D0MH00586J.

39. Yu, B.-B. *et al.* Heterogeneous 2D/3D Tin-Halides Perovskite Solar Cells with Certified Conversion Efficiency Breaking 14%. *Adv. Mater.* 2102055 (2021) doi:10.1002/adma.202102055.

40. Jiang, X. Ultra-high open-circuit voltage of tin perovskite solar cells via an electron transporting layer design. *Nat. Commun.* 7 (2020).

41. Choi, Y. C., Lee, D. U., Noh, J. H., Kim, E. K. & Seok, S. I. Highly Improved Sb2S3 Sensitized-Inorganic–Organic Heterojunction Solar Cells and Quantification of Traps by Deep-Level Transient Spectroscopy. *Adv. Funct. Mater.* **24**, 3587–3592 (2014).

42. Wu, C. *et al.* Water Additive Enhanced Solution Processing of Alloy Sb2(S1−xSex)3-Based Solar Cells. *Sol. RRL* **4**, 1900582 (2020).

43. Huber, S. P. *et al.* AiiDA 1.0, a scalable computational infrastructure for automated reproducible workflows and data provenance. *Sci. Data* **7**, 300 (2020).

44. Kresse, G. & Hafner, J. Ab initio molecular dynamics for liquid metals. *Phys. Rev. B* **47**, 558–561 (1993).

45. Kresse, G. & Furthmüller, J. Efficiency of ab-initio total energy calculations for metals and semiconductors using a plane-wave basis set. *Comput. Mater. Sci.* **6**, 15–50 (1996).

46. Kresse, G. & Furthmüller, J. Efficient iterative schemes for ab initio total-energy calculations using a plane-wave basis set. *Phys. Rev. B - Condens. Matter Mater. Phys.* **54**, 11169–11186 (1996).

47. Blöchl, P. E. Projector augmented-wave method. *Phys. Rev. B* **50**, 17953–17979 (1994).

48. Zunger, A., Wei, S.-H., Ferreira, L. G. & Bernard, J. E. Special quasirandom structures. *Phys. Rev. Lett.* **65**, 353–356 (1990).

49. van de Walle, A., Asta, M. & Ceder, G. The alloy theoretic automated toolkit: A user guide. *Calphad* **26**, 539–553 (2002).

50. van de Walle, A. *et al.* Efficient stochastic generation of special quasirandom structures. *Calphad* **42**, 13–18 (2013).

51. Geller, S. & Wernick, J. H. Ternary semiconducting compounds with sodium chloride-like structure: AgSbSe2, AgSbTe2, AgBiS2, AgBiSe2. *Acta Crystallogr.* **12**, 46–54 (1959).

52. Heyd, J., Scuseria, G. E. & Ernzerhof, M. Hybrid functionals based on a screened Coulomb potential. *J. Chem. Phys.* **118**, 8207–8215 (2003).

53. Borlido, P. *et al.* Exchange-correlation functionals for band gaps of solids: benchmark, reparametrization and machine learning. *Npj Comput. Mater.* **6**, 96 (2020).

54. Krukau, A. V., Vydrov, O. A., Izmaylov, A. F. & Scuseria, G. E. Influence of the exchange screening parameter on the performance of screened hybrid functionals. *J. Chem. Phys.* **125**, 224106 (2006).

55. Skelton, J. *JMSkelton/Transformer*. (2021).

56. Perdew, J. P. *et al.* Restoring the Density-Gradient Expansion for Exchange in Solids and Surfaces. *Phys. Rev. Lett.* **100**, 136406 (2008).

57. Csonka, G. I. *et al.* Assessing the performance of recent density functionals for bulk solids. *Phys. Rev. B* **79**, 155107 (2009).

58. Hoye, R. L. Z. *et al.* Perovskite-Inspired Photovoltaic Materials: Toward Best Practices in Materials Characterization and Calculations. *Chem. Mater.* **29**, 1964–1988 (2017).

59. Huang, Y.-T., Kavanagh, S. R., Scanlon, D. O., Walsh, A. & Hoye, R. L. Z. Perovskite-inspired materials for photovoltaics and beyond—from design to devices. *Nanotechnology* **32**, 132004 (2021).

60. Zheng, Q. *QijingZheng/VaspBandUnfolding*. (2021).

61. Popescu, V. & Zunger, A. Extracting E versus $\vec{k}$ effective band structure from supercell calculations on alloys and impurities. *Phys. Rev. B* **85**, 085201 (2012).

62. D. Whalley, L. effmass: An effective mass package. *J. Open Source Softw.* **3**, 797 (2018).

63. J Jackson, A., M Ganose, A., Regoutz, A., G. Egdell, R. & O Scanlon, D. Galore: Broadening and weighting for simulation of photoelectron spectroscopy. *J. Open Source Softw.* **3**, 773 (2018).

64. Nelson, R. *et al.* LOBSTER: Local orbital projections, atomic charges, and chemical-bonding analysis from projector-augmented-wave-based density-functional theory. *J. Comput. Chem.* **41**, 1931–1940 (2020).

65. Morgan, B. J. vasppy. zenodo.org/record/4460130 (2021) doi:10.5281/zenodo.4460130.

66. Ong, S. P. *et al.* Python Materials Genomics (pymatgen): A robust, open-source python library for materials analysis. *Comput. Mater. Sci.* **68**, 314–319 (2013).

FIGURES

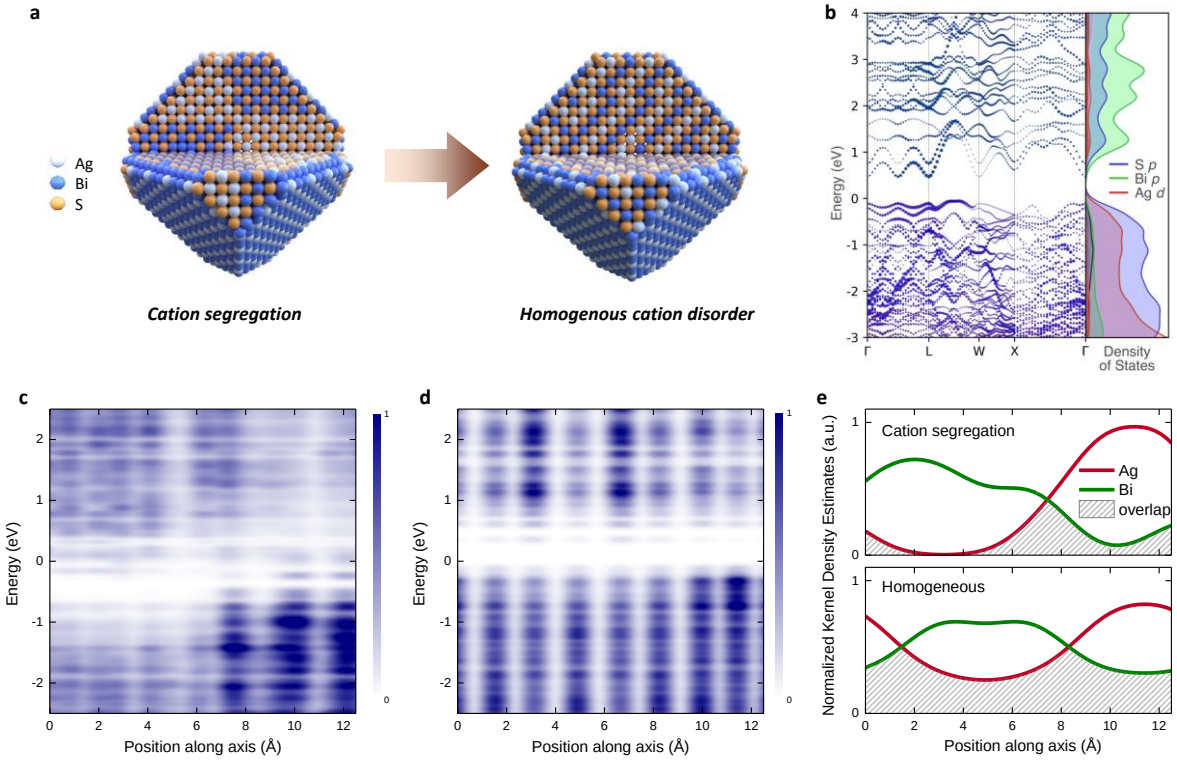

Figure 1. Absorption enhancement via cation disorder homogenisation. a, Schematic of $AgBiS_2$ NCs with cation segregation and homogeneous cation disorder. **b,** Effective electronic band structure of homogeneous disordered $AgBiS_2$, alongside the electronic density of states. Atomic orbital contributions have been projected with the colour map (S *p*: blue, Bi *p*: green, Ag *d*: red). VBM set to 0 eV. **c,** Planar-averaged local electronic density of states (LDOS) for cation segregated $AgBiS_2$. **d,** Planar-averaged local electronic density of states for homogeneous cation disordered $AgBiS_2$. **e,** Normalized Kernel density estimates (KDEs) of Ag and Bi for cation segregation and homogeneous cation disordered $AgBiS_2$. Shadow area shows the overlap of Ag and Bi KDEs.

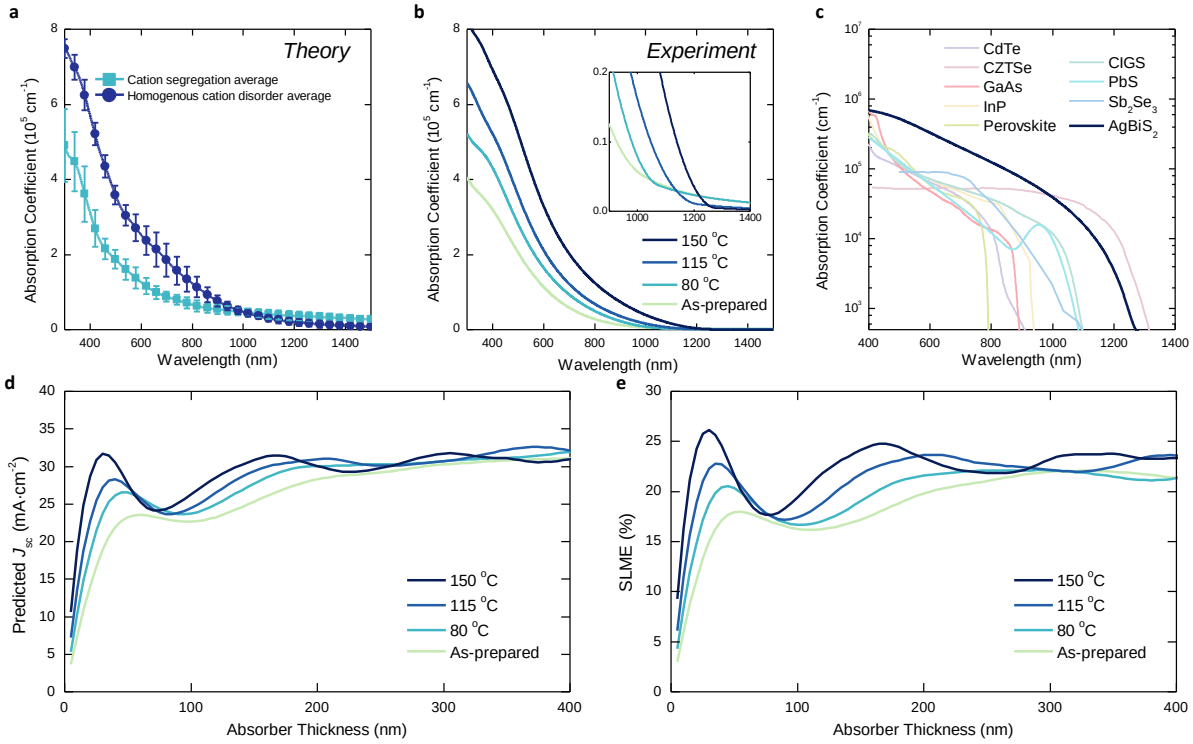

Figure 2. Absorption coefficients and optical modelling. a, Simulated absorption coefficients of $AgBiS_2$ with different cation distributions. Error bars indicate the standard deviation. **b,** Absorption coefficients of $AgBiS_2$ NCs annealed at different temperatures. Inset: Zoom-in of long wavelength region. **c,** Absorption coefficient of $AgBiS_2$ NCs films compared with other photovoltaic materials (CdTe[24], CZTSe[25], GaAs[4], InP[26], Perovskite[27], CIGS[4], PbS, Sb_2Se_3[28]). **d,** Predicted short circuit current density (J_{sc}) of $AgBiS_2$ NCs using the transfer matrix method (TMM). **e,** Spectroscopic Limited Maximum Efficiency (SLME) of $AgBiS_2$ NCs as a function of film thickness.

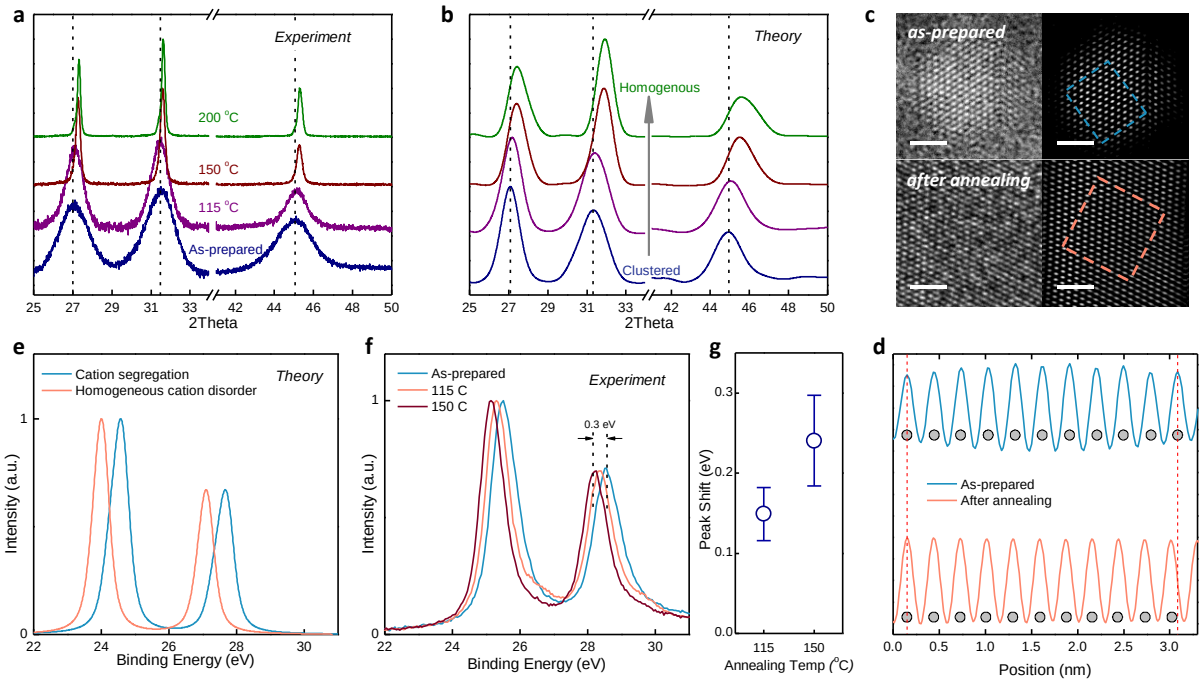

Figure 3. Characterization of cation configuration transition. (Clockwise) a, Experimental XRD patterns of $AgBiS_2$ NCs annealed at different temperatures. **b,** Simulated XRD of 10nm $AgBiS_2$ NCs with varying cation distribution homogeneity, from cation segregation to homogeneous cation disorder. **c,** High resolution transmission electron microscope (HRTEM) images of $AgBiS_2$ NCs before and after 200°C annealing. Scale bar: 2 nm. **d,** Integrated line profiles of the {200} crystal plane indicated by dashed lines in **c**. **e,** Simulated valence band x-ray photoelectron (XPS) spectra of $AgBiS_2$ with different cation configurations. **f,** Experimental XPS spectra of $AgBiS_2$ NCs annealed at different temperatures. Dashed lines indicates the peak positions before and after annealing. **g,** Statistics of XPS peak shifts from three different batches of samples. Error bars indicate the standard deviation.

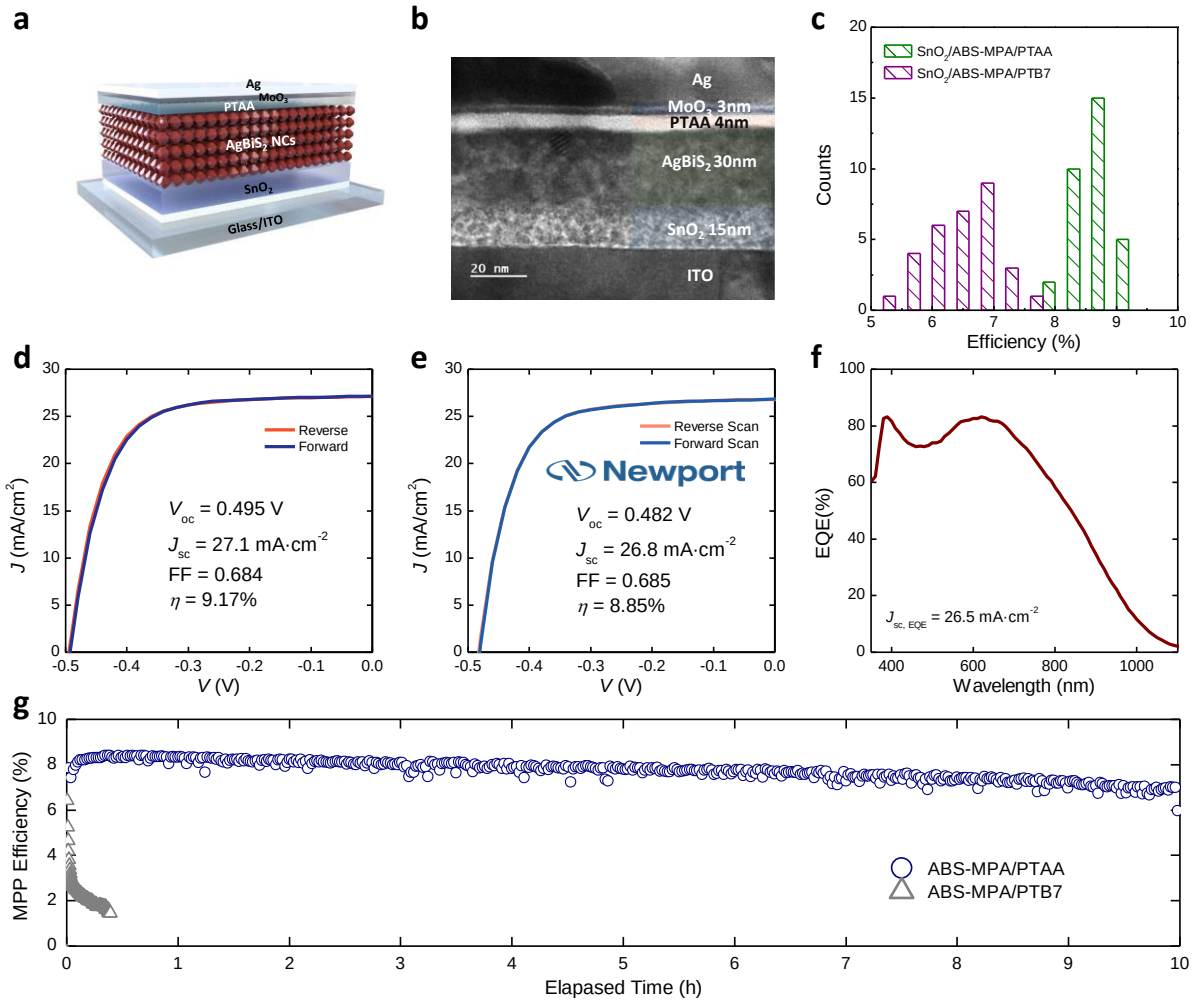

Figure 4. Ultrathin $AgBiS_2$ NCs solar cells. a, Schematic of the $AgBiS_2$ NCs solar cells. **b,** Cross-sectional TEM image of the device. **c,** Statistical histogram of $AgBiS_2$ NCs solar cells with PTB7 and PTAA as hole transport layer (HTL). **d,** *J-V* curves of the champion device with PTAA as HTL. **e,** *J-V* curves of $AgBiS_2$ NCs solar cells certified at Newport, USA. **f,** EQE curve of the champion device. **g,** Maximum power point (MPP) test of $AgBiS_2$ devices with PTB7 and PTAA as HTLs.

601 TABLES

602

603 **Table 1 Photovoltaic parameters of devices based on different hole transport layers**

	V_{oc} (V)	J_{sc} (mA·cm-2)	FF	PCE (%)
$AgBiS_2$ NCs/PTB7	0.437 ± 0.011	25.59 ± 0.81	0.57 ± 0.03	6.42 ± 0.55
Champion device	0.450	26.75	0.63	7.63
$AgBiS_2$ NCs/PTAA	0.489 ± 0.005	26.99 ± 0.76	0.66 ± 0.02	8.70 ± 0.31
Champion device	0.495	27.11	0.68	9.17
Certified	0.482	26.8	0.68	8.85

604 *Note: statistics are based on 31 different devices.*

605

606